

4.2 Bulgeless galaxies hosting growing black holes

The work in the following chapter is in preparation for submission to MNRAS in Simmons, Smethurst & Lintott (in prep.). I assisted in the planning and taking of observational spectral data, along with being responsible for the subsequent data reduction and statistical analysis. I was also a major contributor to the interpretation of the results.

Although the study of large populations of galaxies provides crucial information to constrain the processes governing galaxy evolution, valuable insight can still be discerned from detailed observations of a smaller sample of rare objects.

The strong correlations that exist between black hole mass and velocity dispersion (Magorrian et al., 1998; Merritt & Ferrarese, 2001; Hu, 2008; Kormendy et al., 2011; McConnell et al., 2011), bulge stellar mass (Marconi & Hunt, 2003; Häring & Rix, 2004), and total stellar mass (Cisternas et al., 2011; Simmons et al., 2013) suggest that galaxies co-evolve with their central super massive black holes (SMBH). Since mergers can grow both bulges and black holes these correlations have been interpreted as the result of a few mergers within a Hubble time (Peng, 2007; Hopkins et al., 2008b; Jahnke & Macciò, 2011). A growing black hole must be accreting matter and is therefore observed as an AGN during this time period. Understanding the triggering mechanisms of AGN, which kick-start this process of simultaneous galaxy and black hole evolution and possible subsequent quenching caused by the AGN, is therefore important. However, in Section 4.1, I presented the argument that disc galaxies currently hosting an AGN undergo quenching with very slow rates, unlike the rapid rates found in simulations of mergers. This suggests a secular driven co-evolution of galaxies and their black holes.

A secular co-evolution of galaxy and black hole has been proposed by previous works (Greene et al., 2010; Jiang et al., 2011b; Cisternas et al., 2011; Simmons et al., 2011; Schawinski et al., 2011; Kocevski et al., 2012) and was investigated by Simmons et al. (2013). Simmons et al. studied 13 AGN residing in bulgeless host galaxies, whose accretion histories are assumed to be merger free. This assumption is validated by the fact that simulations have repeatedly shown that mergers with mass ratios larger than 1:10 (i.e. mergers where the mass of the satellite is greater than 10% of the main galaxy's mass) will form a classical bulge (Walker et al., 1996; Hopkins et al., 2012; Tonini et al., 2016). Simmons et al. identified two broad line objects in

their sample from which they calculated black hole masses, and placed lower limits on the black hole masses of the other 11 objects. They found that the black hole masses were larger than predicted by established stellar bulge mass-black hole mass relations, but consistent with total stellar mass-black hole mass relations. However, these conclusions were drawn based on only two direct measurements of black hole mass and so they were limited by small number statistics.

In this study, I follow up the investigation of Simmons et al. by examining a larger sample of disc galaxies which are visually identified as bulgeless AGN hosts and investigate the locations of these galaxies on typical galaxy-black hole scaling relations. Since the disc galaxies in this sample will have different dynamical histories to bulge dominated galaxies, a correlation between their black holes and bulge stellar masses is not expected, if different dynamical histories lead to different mechanisms for black hole growth.

4.2.1 Observational Data

The goal of this study is to investigate black hole growth in galaxies whose growth histories have been dominated by relatively calm, slow processes. A sample of growing (i.e. active) black holes hosted in disc-dominated galaxies is therefore required. Optimally, the AGN should have broad emission lines to facilitate measurement of black hole masses via well-established relations between line flux and width and black hole mass. Simmons et al. used GZ2 to select their sample of bulgeless galaxies which selected against very massive black holes with unobscured emission. This is due to AGN bias, where a bright central point source can mimic a bulge, significantly affecting the bulge classification in Task 4 of the GZ2 decision tree (see Figure 1.5). In an investigation of the addition of a synthetic bright point source to an image of a bulgeless inactive galaxy, Simmons et al. found that a synthetic AGN with a luminosity of just 1/50th of the host galaxy can reduce the $p_{\text{no bulge}}$ classification by at least 50%. The GZ2 classifications are not utilised in this study for this reason. The aim is instead to select AGN hosted in bulgeless galaxies at all masses with broad emission lines that can be used to calculate black hole masses through virial assumptions (see Section 4.2.2.1). Below the methods used to select both a disc dominated AGN sample along with a control sample of typical AGN host galaxies are described.

4.2.1.1 Selecting disc-dominated AGN host galaxies

A sample of unobscured AGN with broad emission lines must first be selected. Black hole masses can then be measured from well-established correlations between emission line properties, such as the FWHM of the broadened $H\alpha$ emission line, and black hole masses (e.g., Greene & Ho, 2007; Jiang et al., 2011a; Xiao et al., 2011; Peterson, 2014).

These unobscured AGN have characteristic colours in multi-wavelength imaging, particularly in X-ray, optical and infrared bands (Kauffmann et al., 2003a; Stern et al., 2005; Goulding & Alexander, 2009; Kauffmann & Heckman, 2009; Aird et al., 2012; Mendez et al., 2013; Azadi et al., 2016; Cowley et al., 2016; Harrison et al., 2016). Given the existence of all-sky surveys at many of the wavelengths relevant to the selection of unobscured AGN, it is possible to construct a large sample of sources identified as unobscured AGN with high likelihood.

An initial sample of AGN was selected using the W2R sample of Edelson & Malkan (2012), comprised of 4,316 sources identified using multi-wavelength data from the *Wide-field Infrared Survey Explorer* (*WISE*; Wright et al., 2010), Two Micron All-Sky Survey (2MASS; Skrutskie et al., 2006), and *ROSAT* all-sky survey (RASS; Voges et al., 1999). This multi-wavelength photometric all-sky selection selects unobscured AGN at > 95 per cent confidence (Edelson & Malkan, 2012).

Following this selection of 4,316 sources, galaxies imaged by the Sloan Digital Sky Survey are then further sub-selected. There are 1,844 W2R sources with positional matches having reported coordinates within $3''$ of a source in the SDSS (York et al., 2000) Data Release 8, a fraction consistent with the fractional area of the SDSS versus an all-sky catalog.

Each of the 1,844 SDSS ugriz colour images were then examined by two of my collaborators (Simmons & Lintott) to identify bulgeless disc galaxies on the basis of clearly identifiable spiral arms, bars or obvious edge-on discs. 101 galaxies were identified¹ which I shall refer to as the BULGELESS sample. Figures 4.10 & 4.11

¹137 bulgeless AGN were originally identified; 96 had spectra available from SDSS, 13 were observable in the 2014A semester with the Intermediate Dispersion spectrograph on the Isaac Newton Telescope, La Palma, Canary Islands, for which observing time was granted, with 5 $H\alpha$ detections made. 28 were observable in the 2014B semester for which observing time on the INT was rejected. Observations of these remaining galaxies currently without spectra, are ongoing at the Kast Double Spectrograph on the Shane 3m telescope at the Lick Observatory, California, USA.

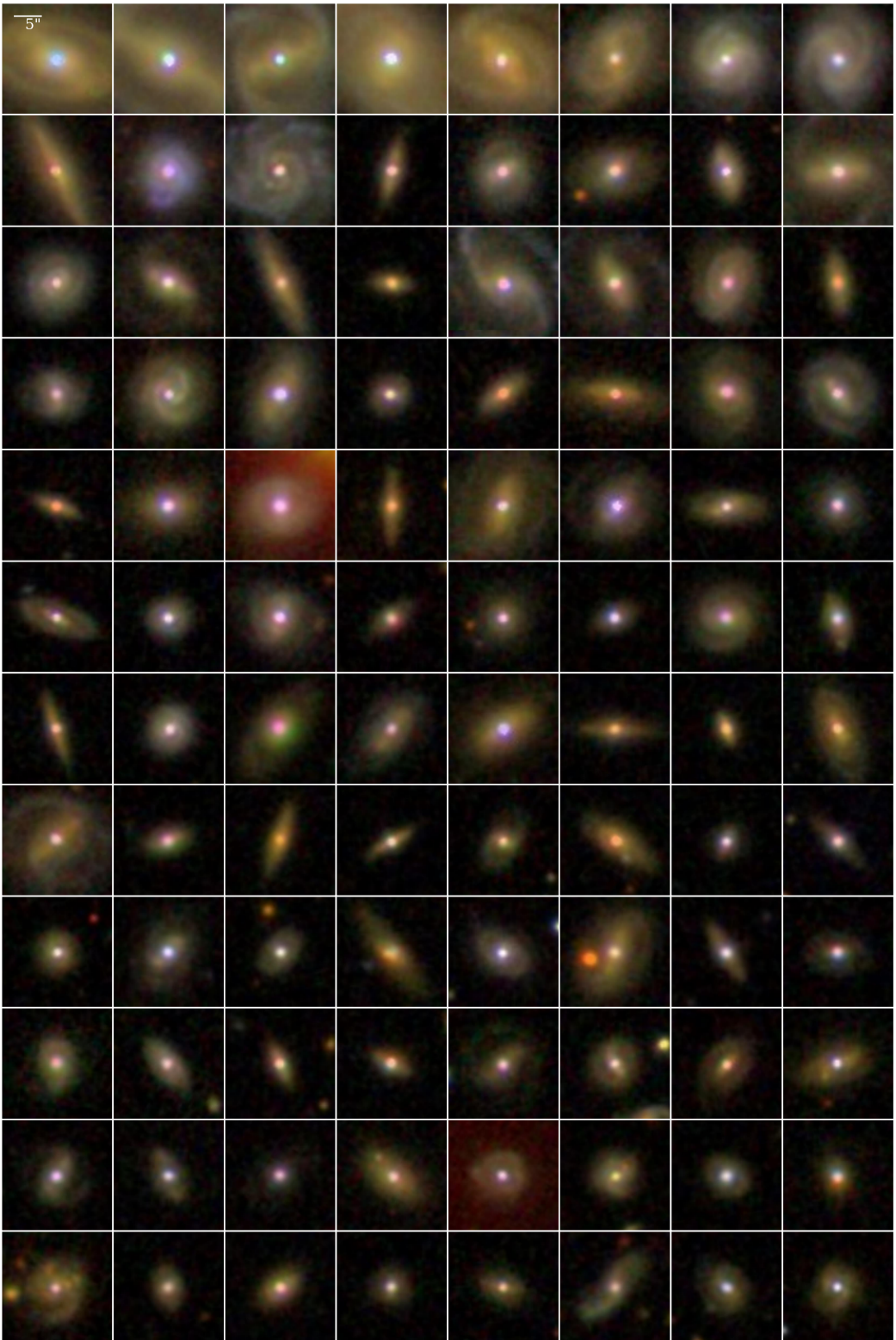


Figure 4.10: Postage stamp SDSS images of the 96 galaxies within the BULGELESS sample for which SDSS spectra were available, sorted from lowest redshift ($z = 0.03$; top left) to highest redshift ($z = 0.24$; bottom right). The scale for each image is shown by the $5''$ ruler in the top left panel.

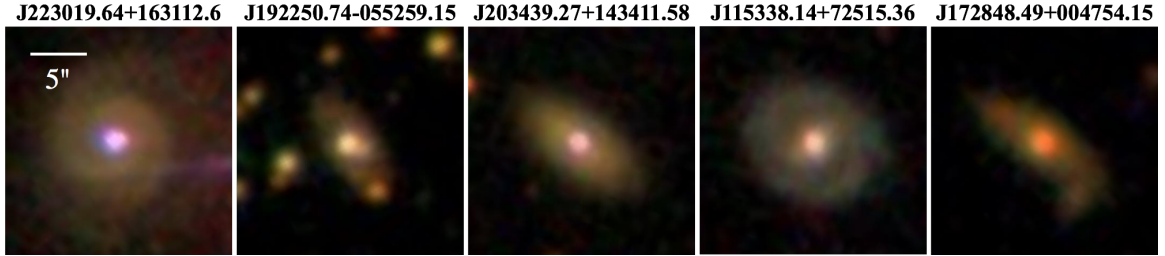


Figure 4.11: Postage stamp SDSS images of the 5 galaxies observed with the IDS on the INT within the BULGELESS sample. The scale for each image is shown by the 5" ruler in the left panel.

collectively show the SDSS postage stamps for all galaxies in the sample, with all images showing the expected bright nebular emission of the unobscured AGN.

4.2.1.2 Spectra

Of the 101 disc-dominated AGN host galaxies with SDSS imaging, 96 have spectra from SDSS Data Release 9 (Ahn et al., 2012), 23 of which were first identified as AGN by Shen et al. (2008) and Edelson & Malkan (2012). Example spectra centred around the broad $H\alpha$ emission at 6562Å for 5 of these SDSS galaxies are shown in Figure 4.12.

The broad $H\alpha$ emission for 5 additional sources was measured using long-slit spectra² techniques with the Intermediate Dispersion Spectrograph (IDS) on the Isaac Newton Telescope (INT) from 21st-23rd May 2014. I reduced these spectra using the standard reduction pipeline of Massey, Valdes & Barnes (1992) using IRAF modules to debiase, dark subtract, flat field, calibrate, sky subtract, flux calibrate and finally extract spectra for the central regions of each galaxy. The redshift of these sources was also measured from the reduced spectra, using the peak of the broadened $H\alpha$ emission to measure λ_{obs} . These reduced spectra, centred around the broad $H\alpha$ emission at 6563Å, are shown in Figure 4.13 with calculated redshifts for the 5 galaxies observed.

²Long slit spectra allows for the measurement of galaxy properties, such as stellar velocity dispersion and SFR, from the extracted galaxy spectrum. This is not possible using the fibre spectra provided by SDSS which only cover the central region of a galaxy. A study of the $M_{BH}-\sigma$ relation will be possible when more long-slit spectra of bulgeless AGN hosts are obtained in the future using the Kast Double Spectrograph.

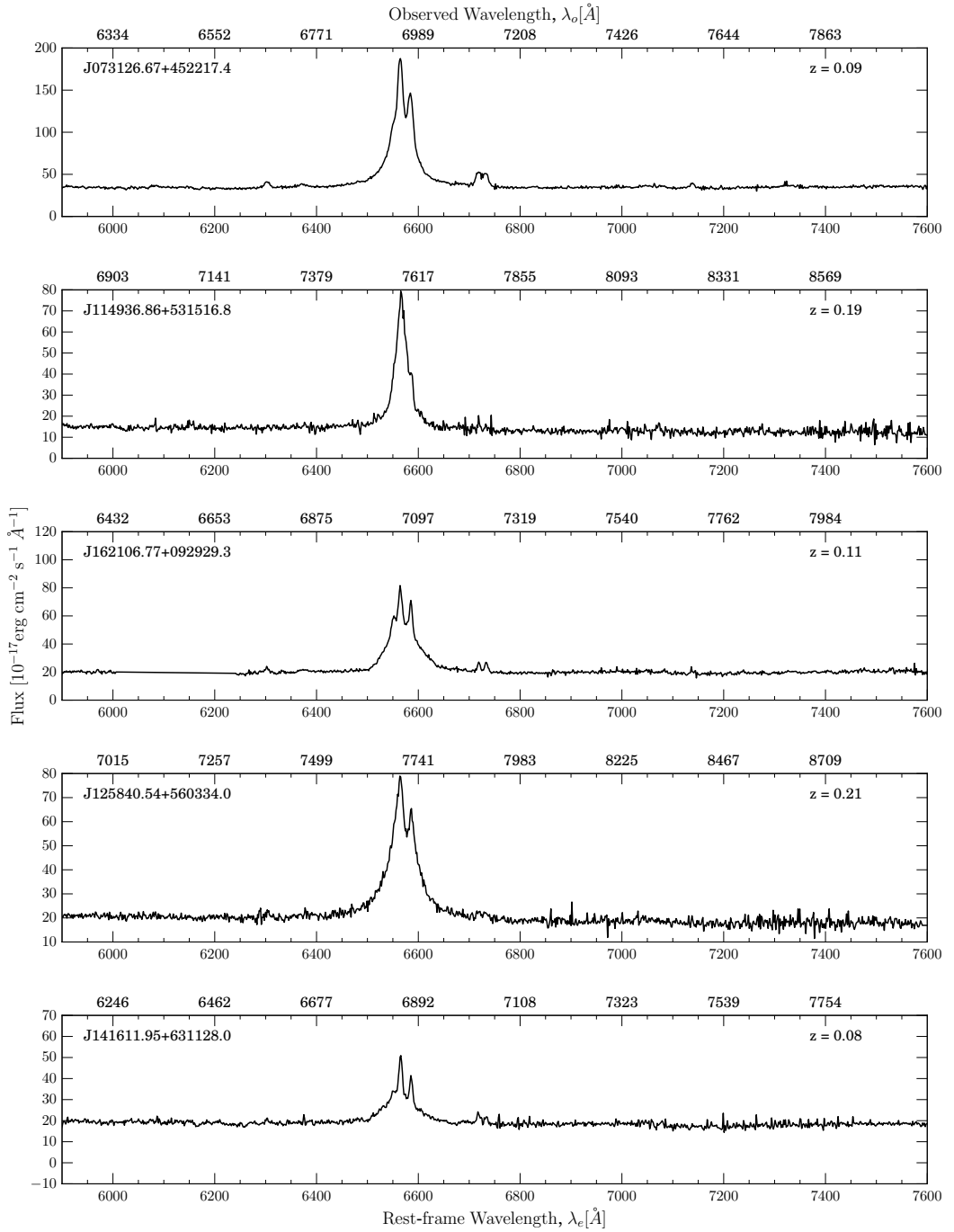


Figure 4.12: 5 example SDSS spectra from with the corresponding measured redshift values shown. Each panel shows the same rest-frame wavelength range (bottom axis of each panel); observed wavelengths are shown on the top axis of each panel. All spectra show broadened $H\alpha$ emission, confirming that the multi-wavelength AGN selection employed here efficiently selects unobscured AGN.

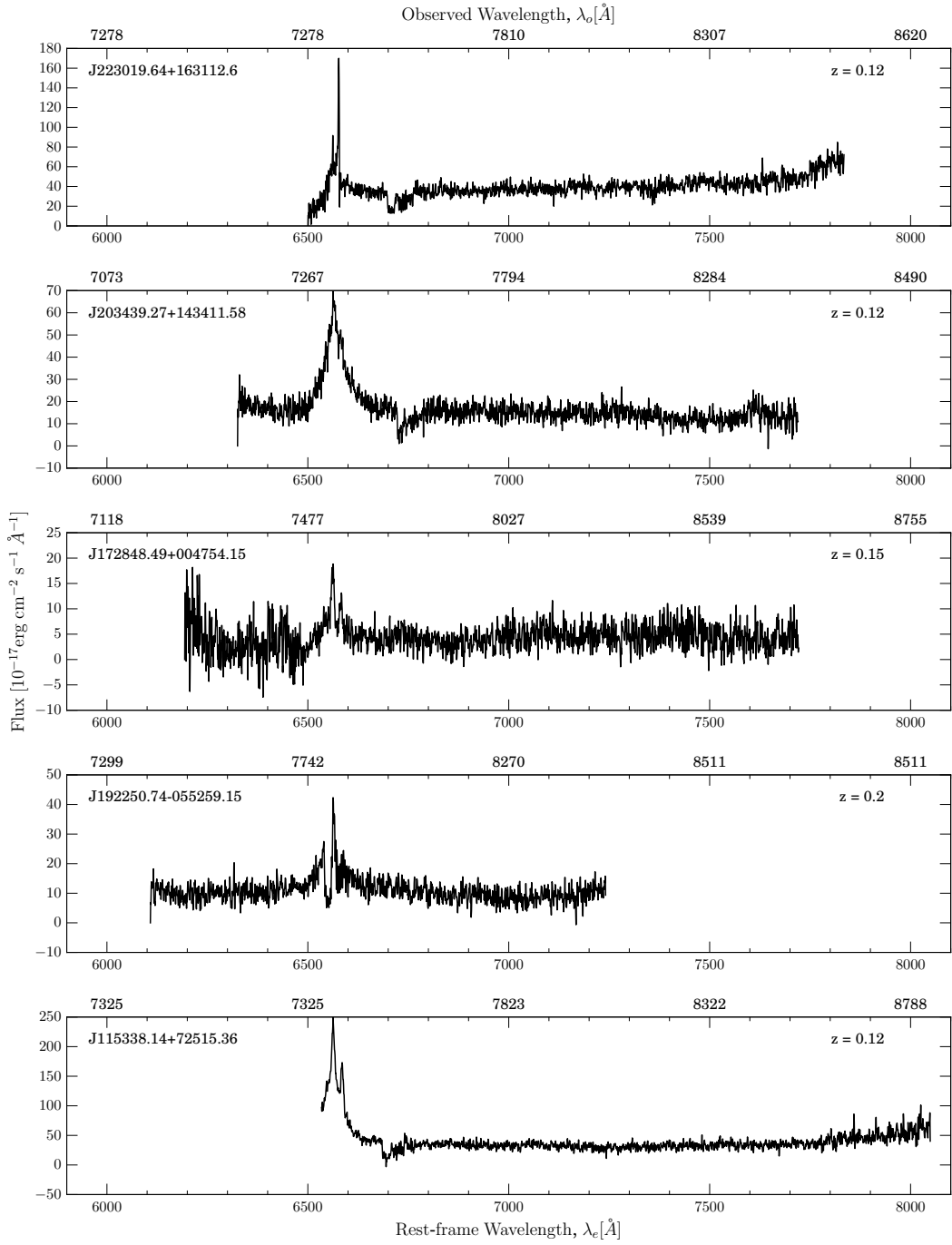


Figure 4.13: Reduced spectra from the IDS on the INT for the 5 galaxies observed. Each panel shows the same rest-frame wavelength range (bottom axis of each panel); observed wavelengths are shown on the top axis of each panel, with redshifts in the top right of each panel. All spectra one again show broadened $H\alpha$ emission, confirming that the multi-wavelength AGN selection employed here efficiently selects unobscured AGN.

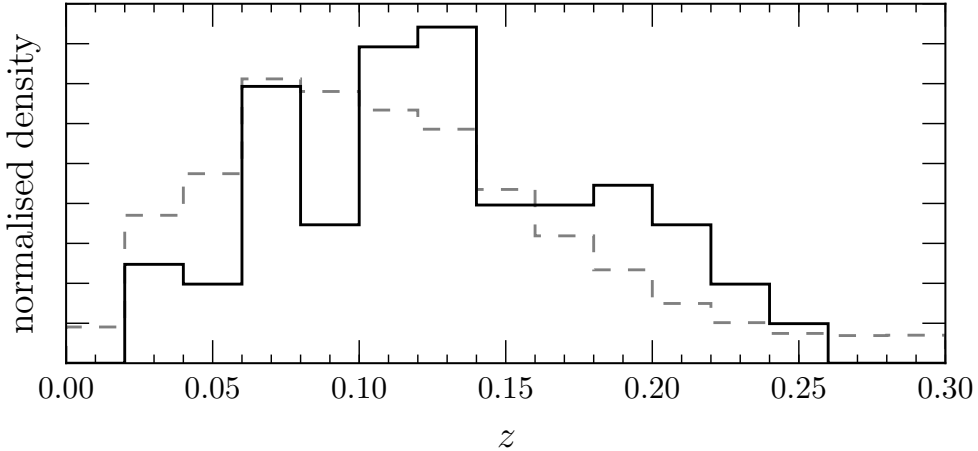


Figure 4.14: Normalised redshift distribution for all 101 sources (solid) for which we have spectra, either from SDSS or measurements with the IDS on the INT. Also shown is the overall redshift distribution of SDSS DR7 in the relevant redshift range of our sources (dashed).

Figure 4.14 shows the redshift distribution of all 101 sources for which we have spectra; the mean redshift of the sample is $\langle z \rangle = 0.129$, with the highest-redshift source having $z = 0.244$.

4.2.1.3 Selecting a Control Sample

Since the majority of the galaxies in the BULGELESS sample have been observed using SDSS, I constructed a control sample from the SDSS quasar catalog of Shen et al. (2011). Using this sample I compiled a sample of 191 galaxies which were redshift matched to within $\pm 5\%$ of the BULGELESS sample. 7 of these galaxies were already part of the BULGELESS galaxy sample and so these were removed. I shall refer to the remaining 184 galaxies as the QSOCONTROL sample. 124 of the QSOCONTROL sample also had measured $(B/T)_r$ ratios from Simard et al. (2011, matched with a $3''$ search radius, see Section 4.2.2.4; see also the middle panel of Figure 4.17 for a comparison of $(B/T)_r$ in the BULGELESS and QSOCONTROL samples).

This provides a control sample of ‘typical’ AGN host galaxies representative of the population in the redshift range probed in this study.

4.2.2 Galaxy and Black Hole Properties

In order to study the relation between the galaxies and their SMBHs in these disc dominated systems, their properties shall be compared to well-tested black hole-galaxy scaling relations. In the following section I therefore describe how the black hole masses, bolometric luminosities, Eddington ratios, photometry and total & bulge stellar masses were derived for each galaxy in the BULGELESS sample.

4.2.2.1 Black hole mass estimates

My goal is to estimate black hole masses independently of galaxy properties, such as σ , in order to compare them with established black hole-galaxy scaling relations. Thus, I instead utilise the established correlation between the black hole mass and the FWHM and luminosity in the broad H α line of Greene & Ho (2007):

$$M_{BH} = (3.0^{+0.6}_{-0.5}) \times 10^6 \left(\frac{L_{H\alpha}}{10^{42} \text{ erg s}^{-1}} \right)^{0.45 \pm 0.03} \left(\frac{\text{FWHM}_{H\alpha}}{10^3 \text{ km s}^{-1}} \right)^{2.06 \pm 0.06} M_\odot, \quad (4.5)$$

derived using a virial assumption. Using this virial assumption for the estimation of black hole masses is facilitated by the selection of unobscured AGN. Unobscured AGN have broad emission lines originating from within the black hole sphere of influence; this photoionized broad line region (BLR) can be used as a dynamical tracer of the black hole mass. The virial black hole mass (Peterson, 2014) can be expressed simply as:

$$M_{BH} = f \frac{R \Delta v^2}{G}, \quad (4.6)$$

where Δv is the velocity dispersion of the emitting BLR, which is assumed to be spherical with radius R . The factor, $f = 0.75$ (Netzer, 1990) then corrects for this simplifying assumption. The velocity dispersion of the BLR can be inferred from the FWHM of a broad line, such as $H\alpha$ or $H\beta$, and the radius inferred from the luminosity of the same broad line. This radius-luminosity relationship is calibrated using the more precise black hole mass measurement technique of reverberation mapping (Blandford & McKee, 1982; Peterson, 2001; Barth et al., 2015) in which the radii are measured based on the observed delay between variations in the AGN continuum and the BLR emission (Kaspi et al., 2005; Bentz et al., 2006). Black hole masses derived with the virial method, under these simplifying geometric assumptions, have been shown to be accurate to within a factor of ~ 3 when compared to masses derived

using the $M_{BH}-\sigma$ method (Ferrarese et al., 2001; Nelson et al., 2004; Onken et al., 2004, and see Section 4.1.1).

To obtain an estimate of the FWHM of the broadened $H\alpha$ lines, I performed spectral fitting on each of the SDSS and INT spectra described in Section 4.2.1.2 to recover narrow- and broad-line strengths and widths of the $H\alpha$ 6563 Å line, by using **GANDALF** (Sarzi et al., 2006) to fit multiple simultaneous lines as well as the continuum of the spectra. **GANDALF** is optimised for use with SDSS spectra and so using the program with the INT spectra required minimal data re-formatting; I logarithmically re-binned and de-redshifted the spectra. From the continuum-subtracted best fit provided by **GANDALF**, I determine the FWHM and line flux of the broad and narrow components of the $H\alpha$ line simultaneously, once again employing **emcee**³, the Python MCMC ensemble sampler by Foreman-Mackey et al. (2013), described in Chapter 2.

The uncertainties reported by **emcee** include an estimate of the uncertainty due to the separation of the narrow and broad line components in the $H\alpha$ emission. The reported uncertainties on black hole masses include this source of uncertainty as well as the reported uncertainties in the black hole-broad line relation (Greene & Ho, 2007). There are other sources of uncertainties, such as those involved in implicitly assuming the fixed geometric correction factor, $f = 0.75$ (Netzer, 1990) for each SMBH, the spectral noise, and the error introduced by assuming a Gaussian line profile for all measured broad lines. Determining uncertainties for the last two is outside the scope of this study; based on visual inspection of the line fits, the first is very small compared to the other uncertainties. These fits to the broad and narrow line $H\alpha$ components in the INT spectra are shown in Figure 4.15.

The black hole masses for the 101 galaxies of the BULGELESS sample range from $10^6 M_\odot \leq M_{BH} \leq 2 \times 10^9 M_\odot$ and the distribution is shown in the left panel of Figure 4.17 in comparison to those from the QSOCONTROL sample.

4.2.2.2 Bolometric Luminosities

Bolometric luminosities are calculated from the wavelength-dependent bolometric corrections shown in Figure 12 of Richards et al. (2006) using the conversion from the

³dan.iel.fm/emcee/

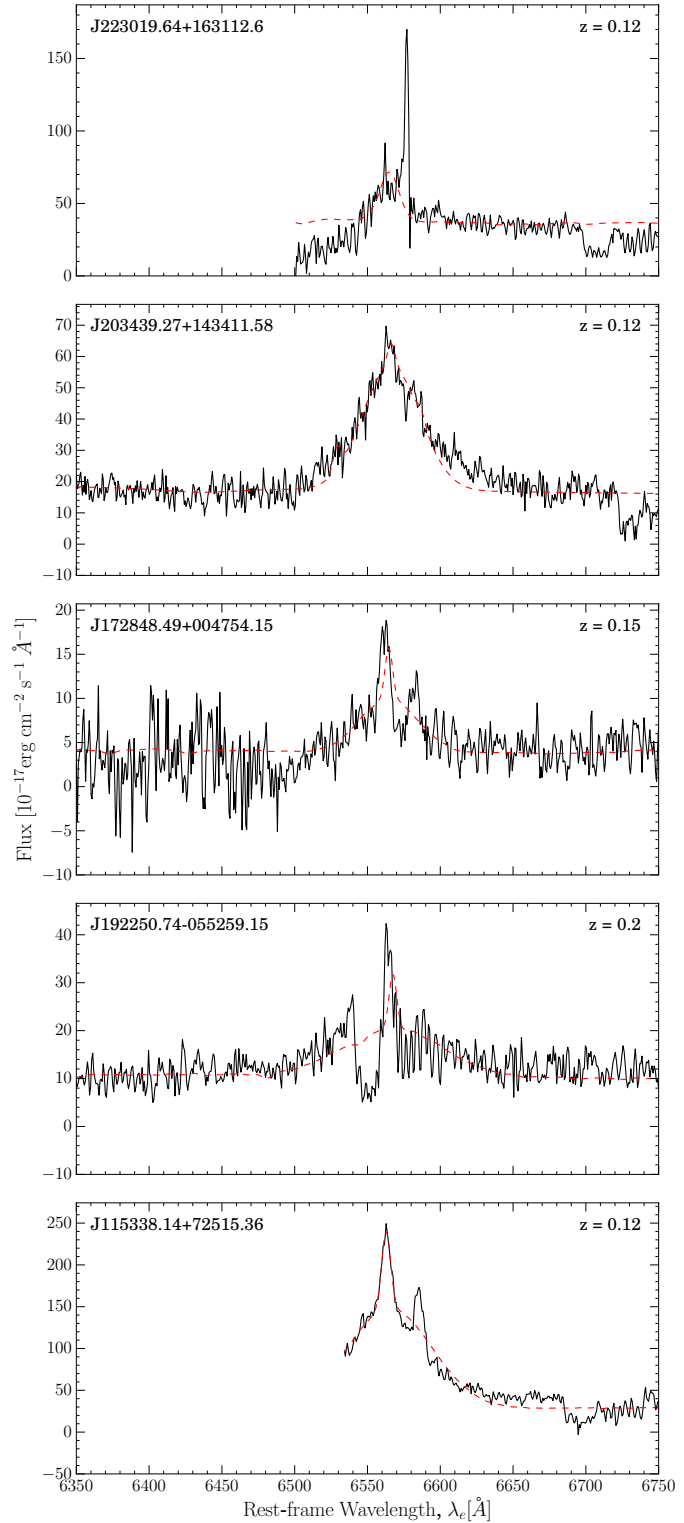


Figure 4.15: Reduced spectra from the IDS on the INT for the 5 galaxies observed with the corresponding measured redshift values shown. Spectra are aligned with the broad $H\alpha$ emission line, the gaussian fits to which are shown by the dashed red line.

$12\mu m$ infrared luminosities, $L_{12\mu m}$:

$$L_{bol} \approx 8 \times L_{12\mu m}. \quad (4.7)$$

The infrared luminosity, $L_{12\mu m}$, is calculated from the WISE W3 magnitudes, M_{W3} , for which all of the BULGELESS sources have a detection, as follows:

$$L_{12\mu m} = \left(\frac{4\pi d^2}{10^{-2} \text{ m}^2} \right) \left(\frac{c}{\lambda} \right) \left(\frac{F_{\nu,0}}{1 \times 10^{23} \text{ Jy}} \right) 10^{\left(\frac{M_{W3}}{-2.5} \right)}. \quad (4.8)$$

The derived bolometric luminosities were first used to calculate Eddington ratios, λ_{Edd} , for the BULGELESS sample (using the method outlined in Section 4.1.1), and then the black hole mass accretion rate, \dot{m} , using a simple matter to energy conversion:

$$L = \frac{E}{t} = \zeta \cdot \frac{mc^2}{t}, \quad (4.9)$$

where $\zeta = 0.15$ (Elvis et al., 2002), is a lower limit⁴ on the radiative efficiency factor (i.e. what fraction of the accreted mass can be turned into radiated energy). The black hole mass accretion rate, \dot{m} is therefore calculated as:

$$\frac{m}{t} = \left(\frac{\dot{m}}{\text{M}_\odot \text{ yr}^{-1}} \right) = \left(\frac{1.58 \times 10^{-26}}{\zeta} \right) \left(\frac{\text{cm s}^{-1}}{c} \right)^2 \left(\frac{L_{bol}}{\text{erg s}^{-1}} \right). \quad (4.10)$$

4.2.2.3 Photometry

The AGN contribution to the magnitude of each galaxy, m_{gal} , is estimated by subtracting the flux in the SDSS `psfMag`, m_{psf} , from the flux in `modelMag`, m_{model} in a given wave band, b as follows:

$$m_{b,gal} = -2.5 \log_{10} \left[10^{\left(\frac{m_{b,model}}{-2.5} \right)} - 10^{\left(\frac{m_{b,psf}}{-2.5} \right)} \right], \quad (4.11)$$

since the normalisation constants in the flux-magnitude conversion will be constant for different sized apertures in a given band. `psfMag` is the best estimate of unresolved emission, while `modelMag` is the optimal quantity for computing aperture-matched source colours⁵. The SDSS `psfMag` is estimated by fitting a single PSF to the point source so that the entirety of the flux in the central PSF is attributed to the AGN. This assumption may therefore overestimate the contribution of the AGN to the

⁴This estimate of the radiative efficiency factor, ζ , is the lowest value necessary to ensure the X-ray background and the black hole energy density are consistent.

⁵<https://www.sdss3.org/dr10/algorithms/magnitudes.php>

central flux. However, given how bright the AGN are in the BULGELESS sample (see Figure 4.17) and how extended the galaxies are (see Figures 4.10&4.11), this effect is assumed to be negligible in this case. A galaxy magnitude, $m_{b,gal}$, is estimated in both the SDSS u and r bands in order to determine the galaxy $u - r$ colour.

A similar NUV galaxy magnitude can be calculated using the GALEX apertures, however matching these apertures to those provided by SDSS cannot be done with a large enough degree of accuracy to derive a reliable galaxy $NUV - u$ colour. This therefore means that STARPY cannot return an accurate SFH for unobscured AGN host galaxies. However, the locations of the BULGELESS sample on the optical colour-magnitude diagram can still be explored; this is studied in Section 5.2 (see Figure 4.22).

4.2.2.4 Total stellar masses

Total stellar masses are calculated using the well-studied relation between stellar mass, absolute galaxy r -band magnitude, $M_{r,gal}$, and $u - r$ galaxy colour (corrected for galactic extinction; Schlegel et al., 1998, using the galaxy magnitudes described in Section 4.2.2.3), following the method of Baldry et al. (2006, see Section ??). Uncertainties are propagated from the colour-magnitude relationship and due to the subtraction of the central AGN component. The average uncertainty on each measurement is ~ 0.3 dex. The distribution of the stellar masses calculated for the BULGELESS sample is shown in the right panel of Figure 4.17.

4.2.2.5 Bulge stellar masses

Calculation of the bulge stellar mass for the BULGELESS sample is more complicated than the total stellar mass calculation described in the previous section. The nuclear emission (as estimated via comparison of `psfMag` to `modelMag`) is generally between 20 to 200 per cent of the entire galaxy-only emission. The presence of the luminous AGN therefore severely compromises the estimates of the bulge-to-total ratio, (B/T), in the host galaxy provided by, e.g., the `fracDeV` parameter reported in the SDSS catalogs. The `fracDeV` parameter estimates that $\sim 80\%$ of the galaxies in this sample are pure de Vaucouleurs (1953) bulges in the r -band, despite the fact that the sample was selected on the basis of clear visual signatures of dominant discs (see Figure 4.10).

None of the photometric parameters derived by the SDSS pipeline allow for the dual presence of an AGN and a host galaxy. Without such considerations the unresolved AGN light is likely to be attributed to the compact bulge component in a bulge-disc model fit (Simmons & Urry, 2008; Koss et al., 2011) leading to an overestimate of the bulge stellar mass.

AGN-host decomposition based on 2-dimensional image fitting (e.g., Simard, 1998; Peng et al., 2002, 2010) is more reliable (e.g. McLure et al., 1999; Urry et al., 2000; McLure & Dunlop, 2001; Sánchez et al., 2004; Pierce et al., 2007; Gabor et al., 2009; Simmons et al., 2011, 2013; Koss et al., 2011). However even in high-resolution *Hubble Space Telescope (HST)* images (Simmons & Urry, 2008) or SDSS imaging at $z \gtrsim 0.06$ (Koss et al., 2011; Simmons et al., 2013) the recovered bulge-to-total ratio can be highly uncertain, particularly for disc-dominated galaxies with a very small bulge or pseudo-bulge (Kormendy & Kennicutt, 2004) component. While the AGN-host decompositions of the galaxies studied by Simmons et al. (2013) recovered reliable bulge-to-total ratios for 11 of the 13 galaxies, their sources were at substantially lower redshift than the BULGELESS sample (with the majority at $z < 0.08$), and their AGN significantly less luminous ($L_{bol} \lesssim 10^{44}\text{erg s}^{-1}$, whereas in the BULGELESS sample $L_{bol} \gtrsim 10^{44}\text{erg s}^{-1}$, see Section 4.2.2.2).

Bulge-to-total fits were first attempted for the 5 galaxies in the BULGELESS sample which were observed with the IDS on the INT using the GALFIT software (Peng et al., 2002); the results of which are shown in Figure 4.16. I used a Sérsic light profile (Sérsic, 1968) to model bulge and disc components, defined by an effective radius, R_e , and light concentration index, n , as:

$$I(R) = I_e \exp \left(-b_n \left[\left(\frac{R}{R_e} \right)^{1/n} - 1 \right] \right), \quad (4.12)$$

where I_e is the intensity at the effective radius, R_e and b_n is a constant defined in relation to the Sérsic index, n . Typical disc light profiles have $n \approx 1$ and bulge profiles have $n \approx 3$. Each of the galaxies observed with the INT were fitted with a disc, bulge and PSF component⁶ (to account for the bright nuclear emission of the AGN). PSFs

⁶Figure 4.11 reveals that at least one of these galaxies may contain a bar, however no bar component is fitted in this procedure. Incorporating a bar component into structural parameter fits has been shown that this is difficult even without the presence of an AGN (Kruk et al., in preparation). Future studies, with higher resolution data (see Section 6.4) will allow for the consideration of a bar component in structural fits.

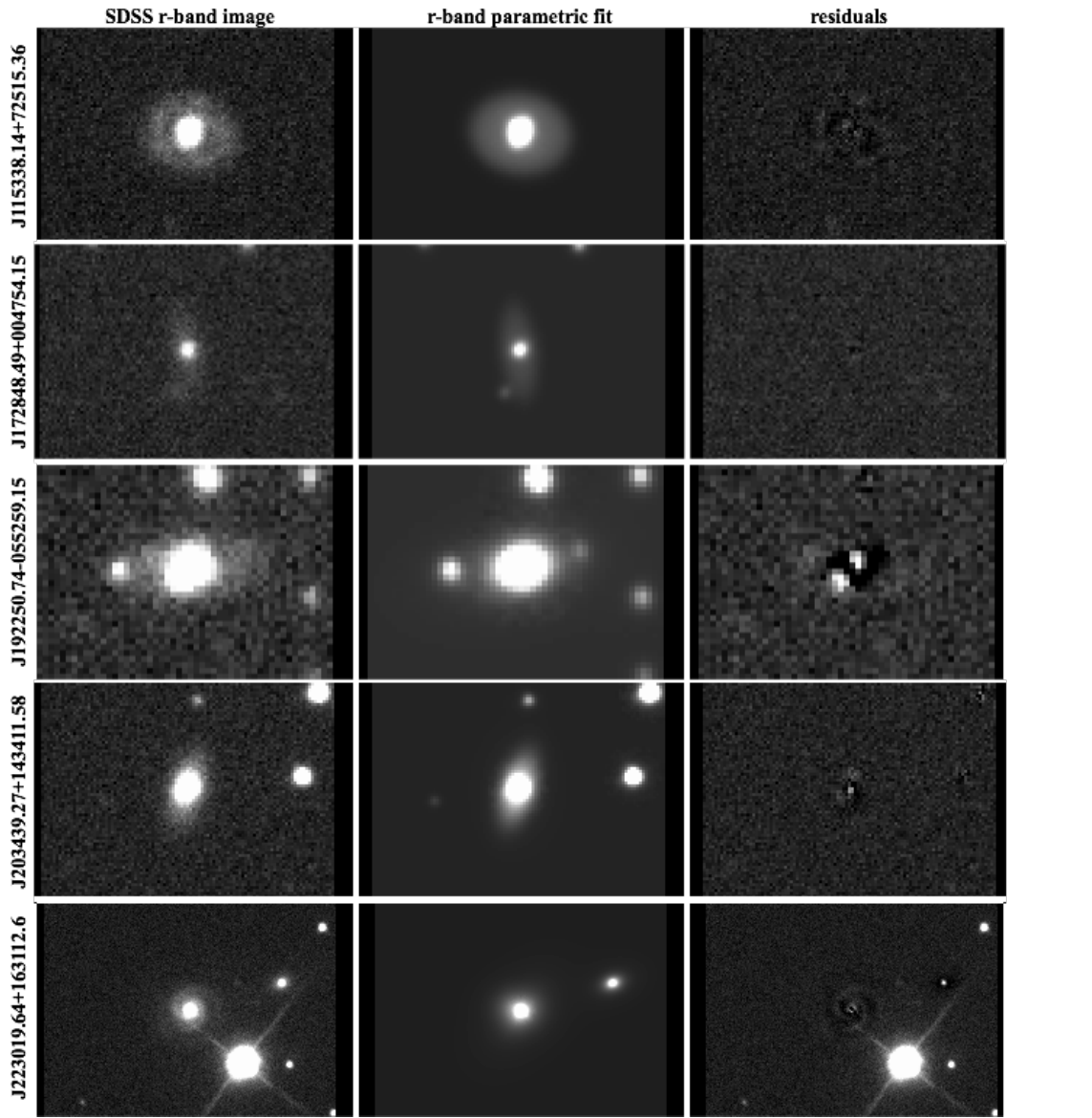


Figure 4.16: SDSS r-band images (left), with the 3 component parametric fits from GALFIT (middle) and the residuals (right; with the same scale as the original image) for the 5 galaxies observed with the IDS on the INT. Stable, but uncertain, bulge-to-total ratios were only recovered for the galaxies in the top two rows. In the bottom three rows the nuclear emission was too bright and image resolution too low to derive a reliable estimate of the bulge-to-total ratio.

were extracted from the SDSS FITS images using the standard `read_PSF` IDL code provided by the SDSS pipeline⁷. Initial guesses of $n = 2.5$ are used on the first pass of the GALFIT algorithm, which uses a χ^2 minimisation method to determine the best fit Sérsic index, effective radius, magnitude and position for each of the disc, bulge and PSF components. This first pass allows the positions of the components to be determined, which are then fixed on a second pass of the algorithm to ensure accurate magnitudes, radii and Sérsic indices are then inferred. From these models, the GALFIT r band magnitudes of the bulge, $m_{r,\text{bulge}}$, and disc, $m_{r,\text{disc}}$, components were used to calculate the bulge-to-total ratio, $(B/T)_r$, as follows:

$$(B/T)_r = \frac{10^{(\frac{m_{r,\text{bulge}}}{-2.5})}}{\left[10^{(\frac{m_{r,\text{bulge}}}{-2.5})} + 10^{(\frac{m_{r,\text{disc}}}{-2.5})}\right]}. \quad (4.13)$$

Highly uncertain bulge-to-total ratios were recovered for only 2 of the 5 galaxies (the top two rows in Figure 4.16). In the remaining 3 cases the nuclear emission was too bright and the image resolution too low for a reliable bulge-to-disc decomposition. Detailed AGN host fits to the SDSS images in the rest of the BULGELESS sample, which lie at similar redshifts, are therefore not likely to produce useful measurements of bulge masses. *HST* imaging would enable these measurements, and although currently not available for the galaxies in this sample, observations are currently underway in Cycle 24 (Proposal ID: 14606, see Section 6.4).

Nevertheless, all we need in this study are conservative upper limits on the bulge masses of the BULGELESS sample. Existing structural parameters from large-scale studies performing bulge-disc decompositions of SDSS galaxies can therefore constrain the maximum possible bulge contribution to the host galaxies. While such studies do not account for the presence of an AGN, their tendency to overestimate the bulge-to-total ratio as a result means that bulge masses derived from these quantities may be taken to be conservative upper limits.

Simard et al. (2011) have already fit multiple models to 1.12 million galaxies in the SDSS catalog to determine best-fit structural parameters for each galaxy. Their r -band bulge-to-total ratio of the best-fit model is taken as an upper limit to the true bulge-to-total ratio of the BULGELESS sample. To convert limits on bulge luminosities to limits on bulge masses, we assume the mass-to-light ratio of the bulge is equal

⁷http://www.sdss.org/dr12/algorithms/read_psf/

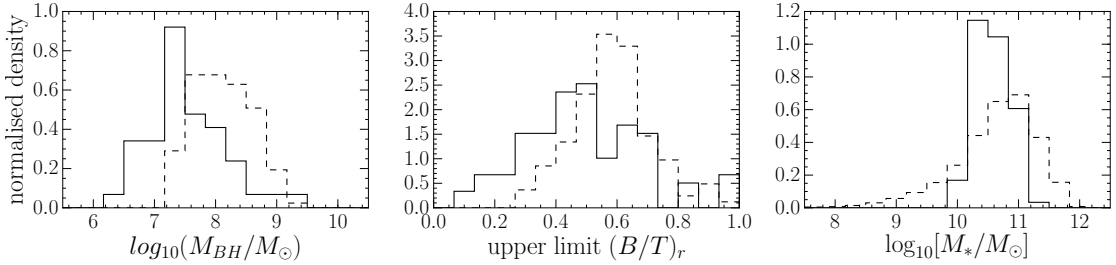


Figure 4.17: Distributions of black hole mass (left), upper limits on the r-band bulge-to-total mass ratio from Simard et al. (2011, middle) and stellar mass (right) of the BULGELESS sample (solid) in comparison to the QSOCONTROL sample (dashed).

to the mass-to-light ratio of the disc. This is a reasonable assumption for disc-dominated galaxies, where many of the “bulge” components, if present, are likely to be rotationally-supported pseudo-bulges (Kormendy & Kennicutt, 2004) with stellar populations similar to that of the disc (Graham, 2001).

The bulge-to-total ratio upper limits of the 89 galaxies in the BULGELESS sample which were included in the Simard et al. (2011) study range from $0.13 \leq (B/\text{Tot})_{r,\max} \leq 1.0$, with a mean value of 0.5. Inspection of the morphologies of the galaxies shown in the images in Figure 4.10 reveals how such a range in $(B/\text{Tot})_{r,\max}$ is clearly an overestimate of the bulge contribution to these galaxies. Applying these bulge-to-total limits to the stellar masses derived in Section 4.2.2.4 results in bulge mass upper limits of $3 \times 10^9 M_\odot < M_{\text{bulge}}[M_\odot] < 7 \times 10^{10}$. The distribution of bulge-to-total mass ratios in the BULGELESS sample are shown in the middle panel of Figure 4.17. The bulge-to-total mass ratios and the black hole masses (left panel Figure 4.17) of the BULGELESS sample are smaller in general than the QSOCONTROL sample, however the stellar masses (right panel Figure 4.17) are found within the range of stellar masses estimated for the QSOCONTROL sample.

All of these derived galaxy and black hole properties of the BULGELESS sample will now be used to determine where these galaxies lie on typical galaxy-black hole scaling relations in Section 4.2.3.

4.2.3 Results

The total stellar mass and estimated bulge masses (see Section 4.2.2.4) are plotted against the black hole masses for the BULGELESS sample in Figures 4.18 & 4.19 respectively. I fit a multiple linear regression model to both of these relations using an inference method which encompasses the uncertainties on both x - and y -dimensions and the intrinsic scatter in the data. The full method is outlined in Kelly (2007) and is publicly available as a *Python* module LINMIX⁸. A brief outline of the method is provided below.

A multiple linear regression model assumes a simple linear relationship between two independent variables, x and y , where both variables are unknown, with added noise, ϵ , from an unknown unobserved random variable (e.g. intrinsic scatter, random errors). In the LIMMIX package this is modelled with the following form:

$$\eta = \alpha + \beta * x_i + \epsilon \quad (4.14)$$

$$x = x_i + x_{err} \quad (4.15)$$

$$y = \eta + y_{err}. \quad (4.16)$$

Here α and β are the regression coefficients to be inferred, x_{err} is the error on the measured values x_i , and y_{err} is the error on the measured values η . ϵ is assumed to be normally-distributed, centred around zero, with a variance σ^2 . x_{err} and y_{err} are also assumed to be normally-distributed and centred around zero with variances σ_x^2 and σ_y^2 , respectively and covariance xy_{cov} . This linear regression method can also incorporate the upper limits on the bulge mass measurements of the 89 SDSS galaxies measured by Simard et al. (2011, see Section 4.2.2.4), by treating them as ‘censored values’ (see Section 7.2 of Kelly, 2007), shown by the solid line in Figure 4.19.

Using LINMIX, I also fit to the observations of 30 early-type galaxies from Häring & Rix (2004). This is shown in Figure 4.18 by the red shaded region for the total stellar mass against black hole mass in comparison to the linear regression fit to the BULGELESS sample, shown by the grey shaded region. The two fitted relations are consistent with each other, despite the fact that the early-type galaxies from Häring & Rix have very different evolutionary histories to the galaxies in the BULGELESS sample.

⁸<http://linmix.readthedocs.org/>

Similarly in Figure 4.19 the fit to the upper limits on the bulge stellar mass against the black hole mass of the BULGELESS sample is shown by the grey shaded region in comparison to the fit to the early-type galaxies from Häring & Rix (2004). Since the Häring & Rix galaxies are early-types the same value for the total and bulge stellar masses are used across Figures 4.18&4.19. The fits to the two samples are not consistent with each other with galaxies in the BULGELESS sample, which contain either no bulge or a pseudo-bulge, preferentially lying above the established relationship between black hole and bulge stellar mass shown for the bulge dominated galaxies of Häring & Rix (2004).

I consider how the black hole mass relates to the black hole accretion rate (estimated using Equation 4.10) of the BULGELESS sample, compared with the QSOCONTROL sample in Figure 4.20. The galaxies of the BULGELESS sample have both lower black hole masses and lower accretion rates in comparison to the QSOCONTROL sample and these are lower in proportion such that the Eddington ratios are very similar, as shown by the distributions in Figure 4.21. In fact, the Eddington ratios of the redshift matched QSOCONTROL sample are, on average, lower than that for the BULGELESS sample. I performed a Kolmogorov–Smirnov (KS) test on these samples and found that I can reject the null hypothesis that the disc dominated galaxies Eddington ratios are drawn from the same distribution as the QSOCONTROL sample but not for the entire quasar sample of Shen et al. (2011).

Within the QSOCONTROL sample, 108 galaxies were morphologically classified by the Galaxy Zoo 1 project Lintott et al. (2008, 2011). Galaxy Zoo 1 did not ask whether a galaxy was a disc, merely whether a galaxy was spiralling clockwise or anti-clockwise. Therefore we can approximate the likelihood of a galaxy being a disc through the combined spiral vote fraction, p_{CS} , where a higher combined spiral vote fraction indicates a higher likelihood of a galaxy being a disc. All of the 108 galaxies of the QSOCONTROL sample are found to have a debiased combined spiral vote fraction of $p_{CS} < 0.5$ and a mean value of $\langle p_{CS} \rangle = 0.17$. The QSOCONTROL sample is therefore mainly comprised of bulge dominated galaxies (including ellipticals) unlike the BULGELESS sample.

The colour-magnitude diagram for the BULGELESS sample is also shown in Figure 4.22 in comparison to the SDSS sample and green valley definition from Baldry et al. (2004). The unobscured AGN host galaxies of the BULGELESS sample are found across the entirety of this parameter space, however those with higher black

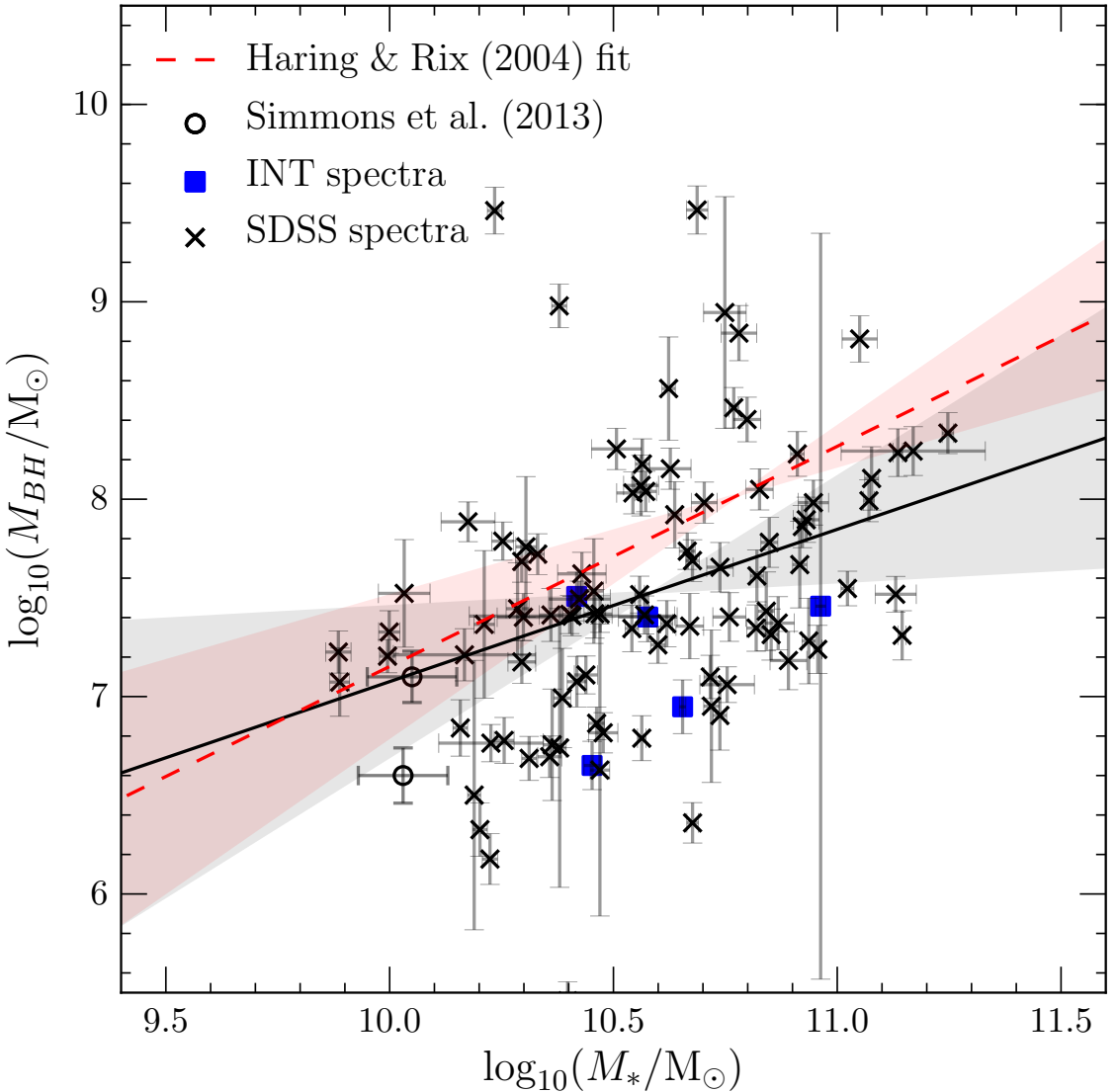


Figure 4.18: Total stellar mass against the black hole mass of the 101 galaxies, including those observed by SDSS (crosses), with the IDS on INT (blue squares) and detections from Simmons et al. (2013, open circles). The best fit line to the data points and two-dimensional errors from linear regression is shown (solid line) with $\pm 3\sigma$ (grey shaded). I also show the best fit found using this same method to the early-type galaxies of Häring & Rix (2004) (dashed line) with $\pm 3\sigma$ (red shaded) and the measured values shown by the red circles. Despite the fact that these galaxies are predominantly disc dominated they are found in the same region of parameter space as the bulge dominated systems used to derive the Häring & Rix (2004) relationship (see discussion in Section 4.2.4).

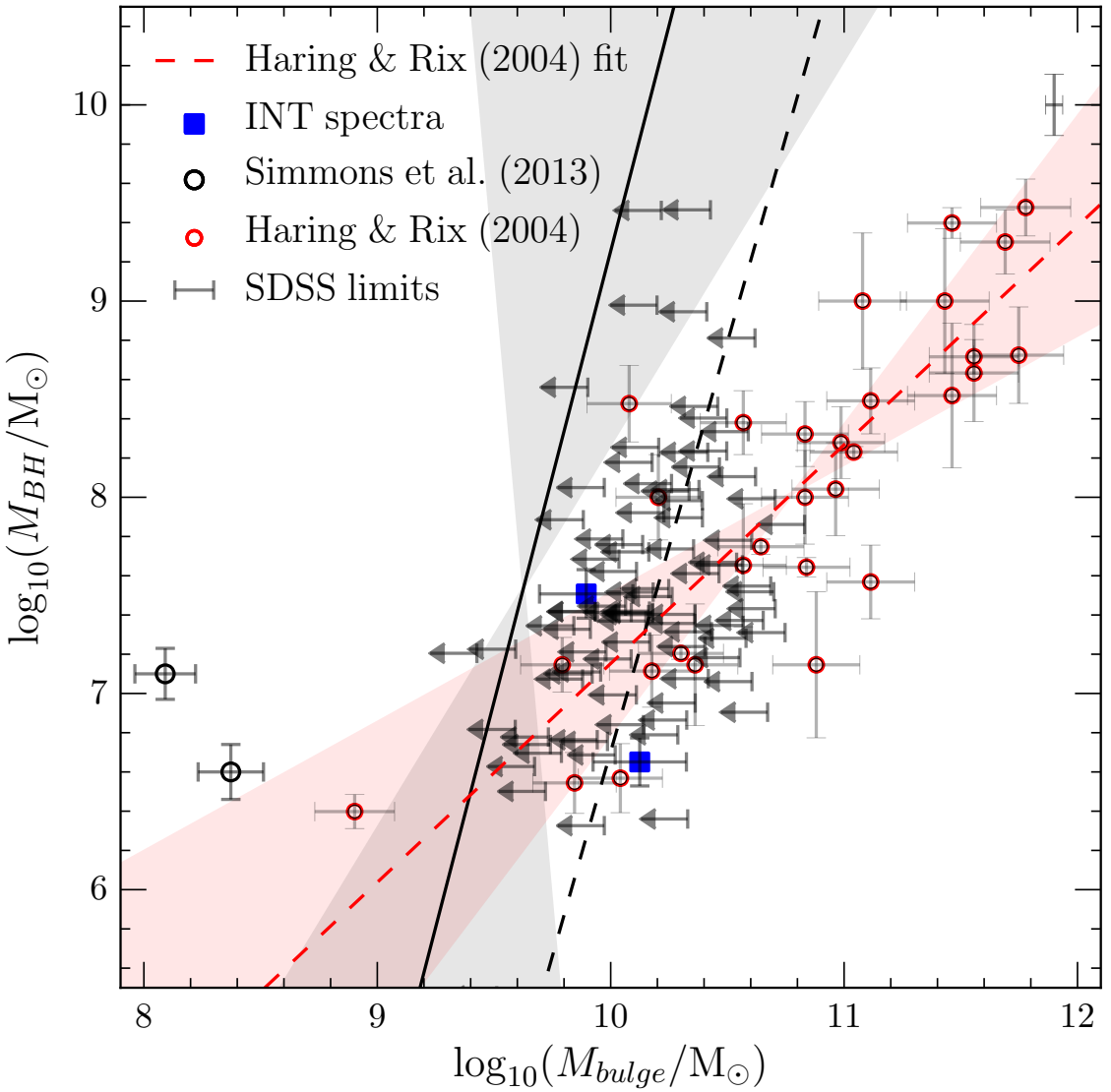


Figure 4.19: The upper limits on the calculated stellar bulge masses are plotted against the black hole mass with the best fit to these upper limits and two-dimensional errors using linear regression methods (solid line) shown with $\pm 3\sigma$ (grey shaded). The dashed line shows the fit if the upper limits are not treated as such. I also show the best fit found using this same method to the early-type galaxies of Häring & Rix (2004) (dashed line) with $\pm 3\sigma$ (red shaded) and the measured values shown by the red circles. Despite the fact that these galaxies are predominantly disc dominated they will are most likely to lie above the Häring & Rix (2004) relationship found for bulge dominated systems (see discussion in Section 4.2.4).

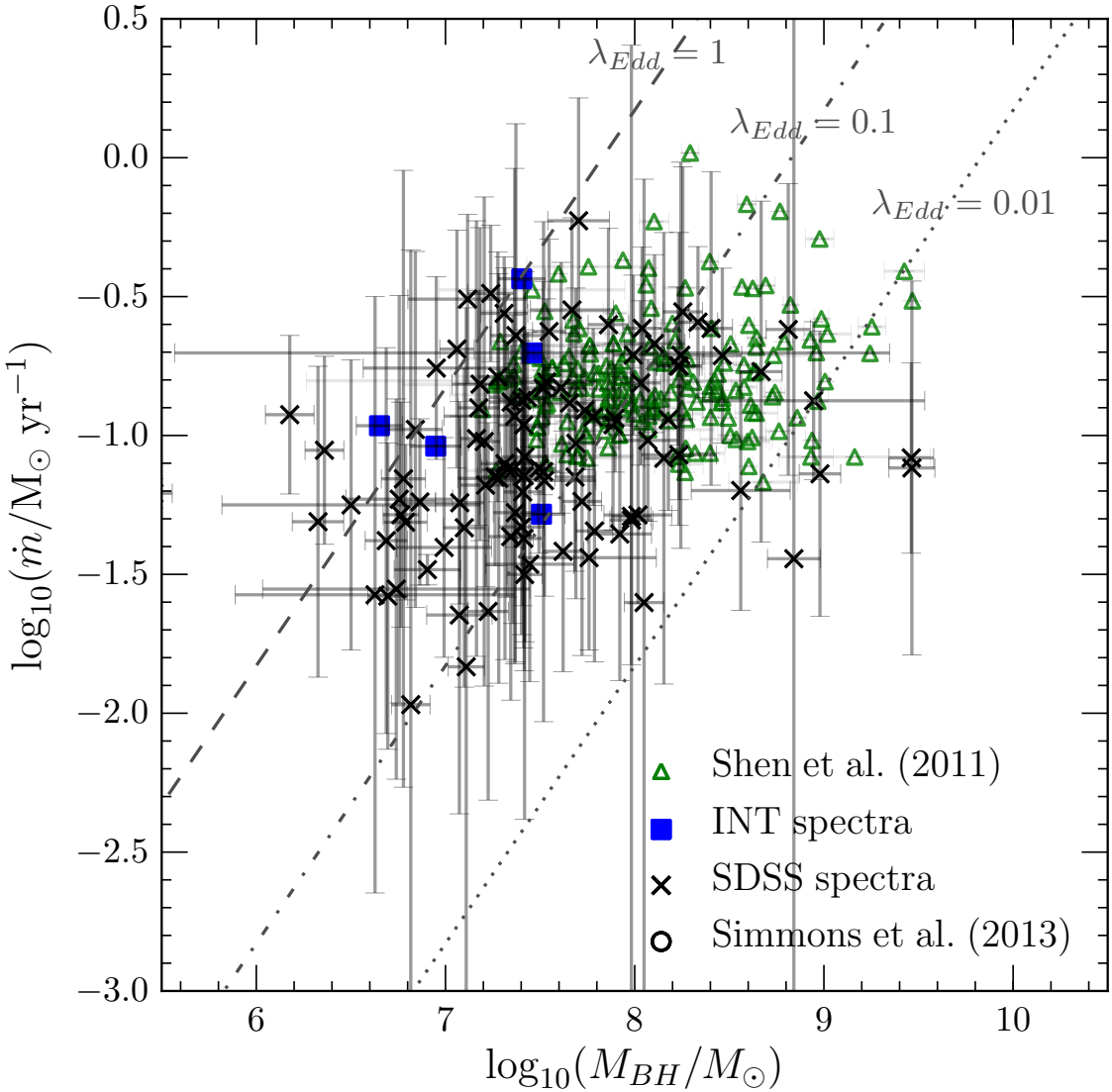


Figure 4.20: Black hole mass against mass accretion rate for the 101 BULGELESS galaxies, including those observed by SDSS (crosses) and with the IDS on INT (squares). We also show detections from Simmons et al. (2013) (open circles) and those from the redshift matched sample of Shen et al. (2011). For reference we show lines of example Eddington ratios of $\Lambda_{Edd} = 1$ (dashed), $\Lambda_{Edd} = 0.1$ (dot-dashed) and $\Lambda_{Edd} = 0.01$ (dotted).

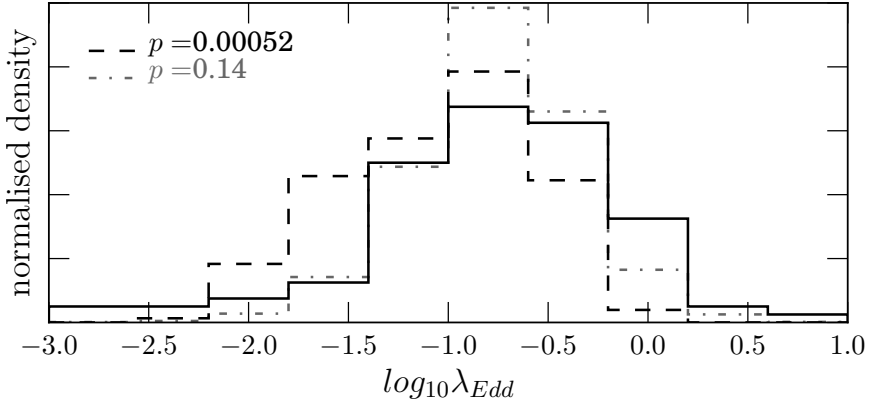


Figure 4.21: Normalised distributions of logarithmic Eddington ratio for the sample of 101 disc dominated galaxies (solid line), compared with that for the redshift matched sample from Shen et al. (2011; dashed line) and the entire SDSS QSO sample (dot-dashed line). I also provide the p-values of a 2 sample KS test between the disc dominated sample and each of the quasar samples. We reject the null hypothesis that the two redshift matched samples are drawn from the same underlying population but cannot reject this hypothesis when comparing the fractional black hole accretion rates of the BULGELESS samples and the entire SDSS QSO sample of Shen et al. (2011).

hole mass accretion rates are found preferentially in the green valley and at brighter r-band magnitudes.

4.2.4 Discussion

The relatively large number of purely disc AGN host galaxies of the BULGELESS sample provide a very powerful probe of the secular driven co-evolution of galaxies and their black holes. Despite the rarity of the morphology of these BULGELESS galaxies, they are found in the areas of black-hole-galaxy scaling relations which are frequented by typical AGN host galaxies of all morphologies, as seen in Figures 4.18, 4.19 & 4.20 (they also lie in the common regions of the local $M_{BH} - \lambda_{Edd}$ plane shown in Figure 1 of the review paper of Alexander & Hickox 2012). Significant black hole growth has occurred up to masses of $M_{BH} \sim 10^8 - 10^9 M_\odot$ in the BULGELESS sample whilst the disc dominated nature of the galaxy has been preserved. Simulations have repeatedly shown that mergers with mass ratios larger than 1:10 (i.e. mergers where

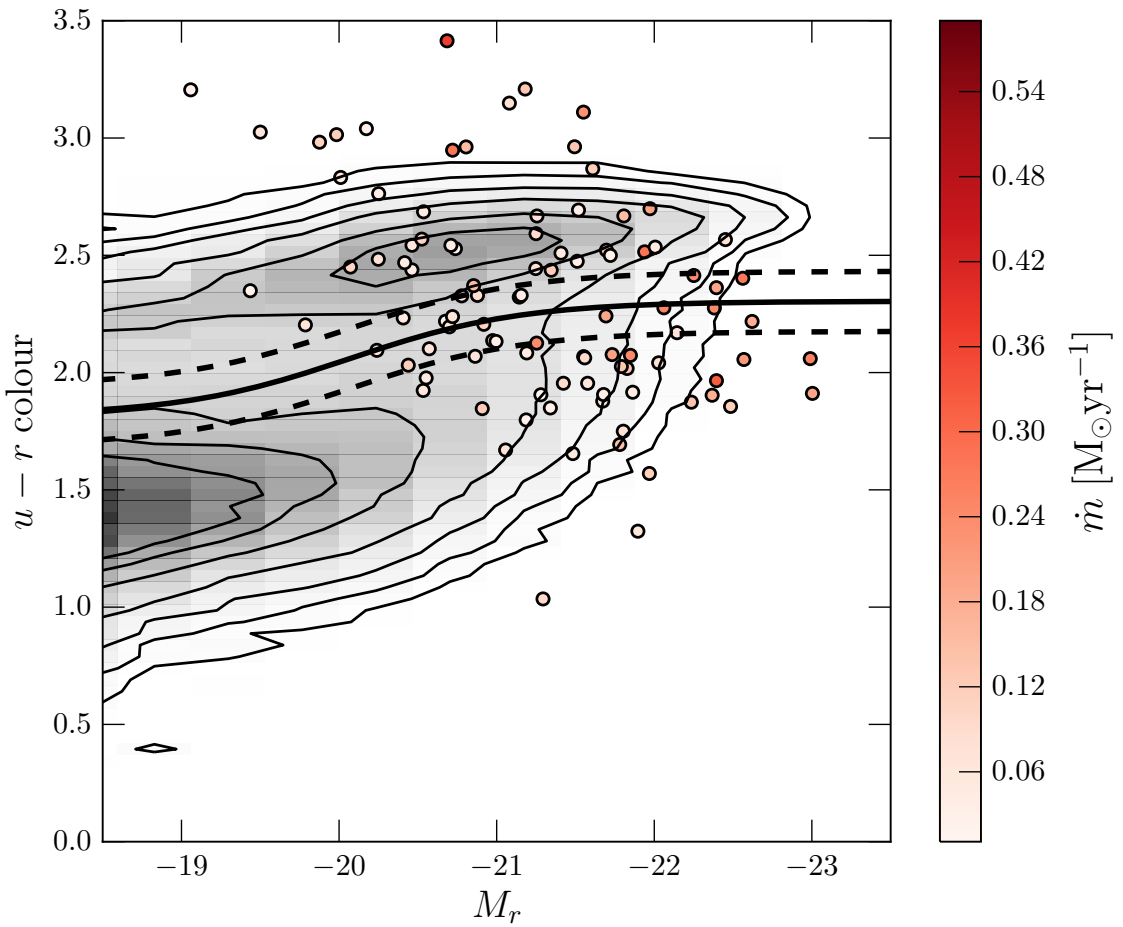


Figure 4.22: Optical colour-magnitude diagram showing the positions of the BULGELESS sample (circles) in comparison to the SDSS DR7 sample from Baldry et al. (2004). The galaxies of the BULGELESS sample are coloured by their black hole mass accretion rate, \dot{m} (see Equation 4.10). The definition between the blue cloud and red sequence from Baldry et al. (2004) is shown by the solid line (as defined in Equation 3.1) with $\pm 1\sigma$ shown by the dashed lines. The BULGELESS sample are found across the colour magnitude diagram, however those with higher mass accretion rates are found preferentially in the green valley and at brighter r-band magnitudes.

the mass of the satellite is greater than 10% of the main galaxy’s mass) will form a classical bulge (Walker et al., 1996; Hopkins et al., 2012; Tonini et al., 2016); so how is this substantial black hole mass growth possible in the absence of such a major merger dominated (and minor merger limited) formation history?

Using Equation 4.10, the black hole mass accretion rates are estimated to lie in the range $0.01 \leq \dot{m} \leq 0.59 M_{\odot} \text{ yr}^{-1}$. Simulations by Crockett et al. (2011), and more recently by Di Teodoro & Fraternali (2014), show that such accretion rates are completely achievable by cold accretion of minor satellites with mass ratios less than 1:10 (i.e. the mass of the satellite galaxy is less than 10% of the main galaxy mass). However, there is also evidence that such accretion rates may also be possible via merger free, secular processes alone. One such secular process, is bar driven gas inflow into the central regions of galaxies. Simulations of barred galaxies have repeatedly shown that gas inflow rates due to the presence of the bar range from $\sim 0.1 - \text{few } M_{\odot} \text{ yr}^{-1}$ (Sakamoto, 1996; Maciejewski et al., 2002; Regan & Teuben, 2004; Lin et al., 2013) and may increase to up to $\sim 7 M_{\odot} \text{ yr}^{-1}$ (Friedli & Benz, 1993) with increasing bar length, bar strength and axis ratio.

These simulations, however, struggle to show that the gas funnelled to the central regions of the galaxy is actually accreted into the central few parsecs, Instead it often accumulates in a nuclear ring wherein it causes a starburst (Regan & Teuben, 2004). Studies of observational correlations between the presence of a bar and that of an AGN often disagree with most finding no correlation at any redshift (Ho et al., 1997; Malkan et al., 1998; Erwin & Sparke, 2002; Lee et al., 2012; Cisternas et al., 2013; Cheung et al., 2015). However Galloway et al. (2015), who take into account that the presence of both an AGN and a galactic bar are strongly correlated with both the stellar mass and integrated colour of the host galaxy, find a small but statistically significant increase of the bar fraction in the AGN host sample. I estimate a bar fraction, f_{bar} , in the BULGELESS sample (which is by no means complete), by visual inspection of the SDSS ugriz images (see Figure 4.10), of $f_{\text{bar}} \sim 0.42$; a lower limit due to the edge on nature of some of the galaxies in the BULGELESS sample. In agreement with the studies above, this is no higher than the local bar fraction observed in the general local galaxy population (Masters et al., 2011) and so I cannot comment on whether the AGN of the BULGELESS sample are being fuelled by bars.

Using the calculated black hole mass accretion rates of the BULGELESS sample, the time required to grow the black holes from a seed mass of $10^2 M_{\odot}$ (Volonteri

et al., 2008) can also be derived. This derivation assumes that the black holes have grown at the currently observed bolometric luminosity, since the mass at which that luminosity was the Eddington luminosity. Prior to this point, they are assumed to have undergone Eddington limited growth. This means that the accretion rates calculated, \dot{m} , will be the maximum rates at which the black holes have grown over their lifetimes (this assumes that the Eddington luminosity is actually an upper limit, however black holes accreting at super-Eddington luminosities have been observed, e.g. Lanzuisi et al. 2016; Pintore et al. 2016; Soria et al. 2016). This is a conservative assumption but gives an estimate of the total time these black holes would need to spend in actively growing phase if the calculated rates are typical of black holes residing in disc dominated host galaxies. The mean time taken for the black holes of the BULGELESS sample to grow from a seed black hole mass is ~ 1.68 Gyr (with a median ~ 0.37 Gyr). These times are considerably less than a Hubble time, with the SMBHs in the BULGELESS sample needing to spend only $\sim 10\%$ of their lifetimes in a growing phase to give the black hole masses currently measured. This is in agreement with the fraction of time predicted by simulations and observed by others for a range of host galaxy morphologies (Kauffmann et al., 2003b; Hao et al., 2005; Hopkins et al., 2006b; Fiore et al., 2012; Simmons et al., 2013).

A time to grow the black hole of ~ 38 Gyr was calculated for two of the most massive black holes in the BULGELESS sample, which have very low current Eddington ratios (see Figure 4.20). Since this time frame is well beyond the current estimates for the age of the Universe (~ 13.8 Gyr; Planck Collaboration, 2016), this value is clearly an overestimate of the time taken to grow these two black holes. We can therefore assume that these two black holes were accreting at a higher rate at some point in their history, supporting the idea of variable AGN accretion rates (Martini & Weinberg, 2001; Yu & Tremaine, 2002; Schawinski et al., 2015). If these two black holes are assumed to have grown within the median time derived for the rest of the BULGELESS sample, then the past accretion rate will have been on the order of, $\dot{m} \sim 7.95 M_{\odot} \text{ yr}^{-1}$ (with a median value $\dot{m} \sim 1.73 M_{\odot} \text{ yr}^{-1}$). As discussed earlier, similar gas inflow rates caused by the presence of a bar have been seen in simulations (Friedli & Benz, 1993); suggesting once again that despite having large masses, these black holes could in theory be grown by secular processes. Unfortunately, the two host galaxies are at too high a redshift to allow the detection of a morphological bar in the SDSS ugriz image.

The black hole accretion rates are also shown in Figure 4.22, where the locations of the BULGELESS sample on the optical colour magnitude diagram are also shown. Those galaxies hosting black holes with higher mass accretion rates are found preferentially in the green valley and at brighter r-band magnitudes. This once again supports the arguments of Section 4.1 that feedback from these AGN could cause galaxies to quench, and therefore transition through the green valley, due to a sustained period of high mass accretion.

The Eddington ratios of the BULGELESS sample are found to be higher than bulge dominated systems in the same redshift range, and instead are consistent with fractional black hole accretion rates occurring at earlier cosmic times (see Figures 4.20 & 4.21). So, despite having merger free evolutionary histories, black hole growth in the BULGELESS galaxies is occurring at a higher rate than in typical local AGN host galaxies. This suggests that secular black hole growth may have been more common at earlier cosmic times. This is supported by the high redshift observations of Georgakakis et al. (2009), Cisternas et al. (2011), Schawinski et al. (2011) and Kocevski et al. (2012) and in the simulations of Hopkins & Hernquist (2006), Bournaud et al. (2011, 2012) which suggest either cold accretion of gas or disk instabilities may have been more dominant than mergers in driving the growth of galaxies at higher redshifts.

If different dynamical histories lead to different mechanisms for black hole growth, the black hole masses of the disc dominated host galaxies in the BULGELESS sample are not necessarily expected to correlate in the same way to their stellar masses as those in bulge dominated galaxies. However, Figure 4.18 shows how the black hole and total stellar masses of the BULGELESS sample occupy the same region of parameter space as the bulge dominated elliptical galaxies used to derive the Häring & Rix (2004) relationship. However, the black hole masses of the BULGELESS sample (which contain either no bulge, or a possible small pseudo bulge) lie well above the bulge mass-black hole relation derived for the Häring & Rix (2004) elliptical galaxies, particularly when the upper limits on BULGELESS bulge masses are taken into account (see Figure 4.19). In other words, if we assume that merger driven processes which grow bulges are the only process responsible for the bulk of black hole growth, the black holes in these disc dominated systems are $\sim 1 - 2$ dex more massive than they should be, given the mass (or lack thereof) of their bulge component. This supports the findings of Simmons et al. (2013) who found a similar excess in the black hole

masses compared to bulge mass upper limits of ~ 1.5 dex and ~ 2 dex for two measured black hole masses.

This finding of overmassive black holes in the BULGELESS sample at first seems contradictory with previous works which found that galaxies with pseudo-bulges have lower black hole masses than predicted by typical scaling relations (see work by Greene et al., 2008; Hu, 2009; Jiang et al., 2011a; Mathur et al., 2012; Ho & Kim, 2014). However, all these studies are biased by their sample selection methods, first selecting based on black hole mass to produce a sample of low mass black holes ($M_{BH} < 10^6 M_\odot$) within which they search for bulgeless or pseudo-bulge morphologies. With the larger in this work, we can see that the fitted relationship between the BULGELESS sample black hole masses and bulge mass upper limits (see Figure 4.19; solid black line), intersects with the relationship derived for the bulge dominated Häring & Rix (2004) sample at $M_{BH} \sim 10^6 M_\odot$. Below this point, the relationship predicts that for disc dominated galaxies the black hole masses will indeed be less than those predicted for bulge dominated systems, as concluded by the studies referenced above.

Splitting the AGN host population by morphology into separate bulge and disc dominated samples, however, leads to biased conclusions. As discussed in Chapter 3, the strength of the POPSTARPY method lies partly in the fact that no thresholds are applied to the GZ morphological vote fractions, allowing the dominance of intermediate quenching rates across the colour magnitude diagram to be revealed (see Section 3.2). Similarly, if we do not “*discriminate*” against morphology in the black hole mass-bulge mass plane and fit a linear regression model to a single galaxy sample consisting of the BULGELESS (with proper consideration of upper limits) and Häring & Rix (2004) samples, the result is consistent with a vertical line in the bulge-black hole mass plane. This suggests that there is perhaps no intrinsic correlation between black hole mass and stellar bulge mass across the full morphological spectrum of galaxies.

Despite the two extremes in galaxy formation histories, the relationships derived in the total stellar mass-black hole mass plane for the BULGELESS and bulge dominated Häring & Rix (2004) samples are consistent with each other (see Figure 4.18). This result, combined with the conclusion that there is perhaps no intrinsic correlation between black hole mass and stellar bulge mass, indicates that the mechanisms driving the dynamical and morphological structure of the galaxy as a whole may not

be fundamental to the growth of the black hole. The black hole-galaxy relations observed across the M_{BH} - σ , M_{BH} - M_{bulge} and M_{BH} - M_* planes, although demonstrating a correlation, have never implied a *causation*. All of these parameters however, share mutual correlations to the overall gravitational potential of the dark matter halo of the galaxy (Booth & Schaye, 2010; Volonteri et al., 2011), suggesting the true cause of the black-hole galaxy scaling relations is an outcome of hierarchical galaxy evolution (Jahnke & Macciò, 2011), regardless of the merger history of the galaxy.

At this point it is tempting to speculate that dark matter may also contribute to the growth of the black hole. This is a valid assumption, since the estimates of the black hole mass in this study are based on a virial assumption. However, in practice, this is incredibly difficult as the dark matter needs to be stripped of its angular momentum before it can be accreted by the black hole. For this reason a prescription for the accretion of dark matter is not incorporated into typical simulations of black hole growth. However, there are a few simulations that investigating this avenue of black hole growth with conflicting results about the validity of such a process (Munyaneza & Biermann, 2006; Peirani & de Freitas Pacheco, 2008; Umeda et al., 2009; Hernandez & Lee, 2010; Guzmán & Lora-Clavijo, 2011; Pepe et al., 2012; Lora-Clavijo et al., 2014). Peirani & de Freitas Pacheco (2008) find that if the dark matter is assumed to undergo adiabatic inflow to the centre of the halo, such a process is possible and may contribute up to $\sim 10\%$ of the accreted black hole mass. Exploring this debatable method of black hole growth may be a possibility in future work studying the methods of black hole growth in bulgeless galaxies.

4.3 Conclusions

In Section 4.1 I used morphological classifications from the Galaxy Zoo 2 project to determine the morphology-dependent SFHs of a population of 1,244 Type 2 Seyfert AGN host galaxies, in comparison to an inactive galaxy population, via a Bayesian analysis of an exponentially declining SFH model. Using POPSTARPY I determined the population densities for the time and exponential rate that quenching occurs and find clear differences in the distributions, between INACTIVE and AGN-HOST galaxy populations and for host galaxies with AGN of different Eddington ratios. The main findings were:

- (i) Quenching at early times is observed within the INACTIVE population (see right panels of Figure 4.7), where the population density is roughly constant until recent times where the distribution drops off at earlier times with increasing mass. This is evidence of downsizing within the INACTIVE galaxy population, which is also seen in the AGN-HOST smooth weighted population. This implies that AGN feedback is not responsible for the cessation of star formation within a proportion of these galaxies, as this quenching has occurred prior to the triggering of the current AGN.
- (ii) Slow, early quenching is also observed in the disc weighted AGN-HOST population (dashed lines bottom left panels of Figures 4.7 & 4.8) and so this SFH challenges the typical merger driven co-evolution of luminous black holes and their host galaxies.
- (iii) Rapid quenching, possibly caused by the AGN itself through negative feedback, is the most dominant history within the low mass (left top panel Figure 4.8) and high Eddington ratio (bottom left panel of Figure 4.6) AGN-HOST population. This quenching history is particularly apparent for the smooth-weighted AGN-HOST population, supporting the hypothesis that a merger, having caused a morphological transformation to a smooth galaxy, can also trigger an AGN, causing feedback and cessation of star formation on rapid timescales (initially proposed in Chapter 3). Further work is required to determine if the AGN is indeed the cause of the quenching seen.
- (iv) The prevalence of star forming AGN host galaxies, combined with the dominance of rapid, recent quenching seen across the AGN-HOST population allows us to consider that either: (i) the AGN are the cause of the rapid quenching observed but only in gas-poor host galaxies where they can have a large impact, (ii) the AGN are a consequence of another quenching mechanism but can also be triggered by other means which do not cause quenching, or (iii) the SFR of a galaxy can recover post-quench and return to the star forming sequence after a few Gyr.

In Section 4.2 I studied how black holes can grow in galaxies with merger free evolutionary histories, by investigating where AGN in disc dominated galaxies lie on typical black-hole galaxy scaling relations. Despite the fact that these disc dominated galaxies have different dynamical histories to bulge-dominated and elliptical shaped

systems, they are found to lie in the same regions of parameter space and are $\sim 1 - 2$ dex more massive than they should be, given the mass (or lack thereof) of their bulge component. The main findings were:

- (i) Significant black hole growth has occurred up to masses of $M_{BH} \sim 10^8 - 10^9 M_\odot$ in the BULGELESS sample whilst the disc dominated nature of the galaxy has been preserved.
- (ii) Eddington ratios of the BULGELESS sample are higher than those in the bulge dominated QSOCONTROL sample. Despite having merger free evolutionary histories, black hole growth in the BULGELESS galaxies is occurring at a higher rate as a fraction of black hole mass than in typical local AGN host galaxies.
- (iii) Those galaxies hosting black holes with higher mass accretion rates are found preferentially in the green valley and at brighter r-band magnitudes. This once again supports the arguments of Section 4.1 that feedback from these AGN could cause galaxies to quench, and therefore transition through the green valley, due to a sustained period of high mass accretion.
- (iv) Figures 4.18 shows how the fitted relationship in the M_* - M_{BH} plane for the BULGELESS sample are consistent with the elliptical galaxies of Häring & Rix (2004). However, in the $M_{\text{bulge}}-M_{BH}$ plane, the black hole masses of the BULGELESS sample lie above the typical relationship for bulge dominated Häring & Rix sample. If we assume that black holes and bulges grow simultaneously in mergers, then the black holes in these disc dominated systems are $\sim 1 - 2$ dex more massive than they should be, given the mass (or lack thereof) of their bulge component. This suggests that there is perhaps no intrinsic correlation between black hole mass and galaxy bulge mass across the full morphological spectrum of galaxies and that the true cause of the black-hole galaxy scaling relations may be due to mutual correlations to the overall gravitational potential of the dark matter halo of the galaxy.

It is therefore clear that AGN can have a large impact on the evolution of their host galaxies, including causing quenching directly through AGN feedback across the entire population; which I have demonstrated here for the first time. However, the external quenching effects driven by the galaxy environment also need to be investigated in order to gain a complete picture of galaxy evolution.